Industrial Engineering Journal
ISSN: 0970-2555
Volume : 53, Issue 9, September : 2024

CONTROL OF HYBRID OFF-GRID CONFIGURATION BASED ON A VARIABLE-SPEED DIESEL GENERATOR WITH FUZZY LOGIC CONTROL STRATEGY

S SAI SUSMITHA[1], S. TARA KALYANI[2]
[1]PG Scholar, Department of Electrical And Electronics Engineering, Jawaharlal Nehru technological University Hyderabad, TS, India email: susmithasuguru21@gmail.com
[2]Senior Member, IEEE, Department of Electrical And Electronics Engineering, Jawaharlal Nehru technological University Hyderabad, TS, India email: tarakalyani@gmail.com

Abstract: A control system must be installed in a hybrid off-grid system that combines a solar photovoltaic array with a diesel engine with variable speed. By combining frame-based and stator flux-oriented approaches to regulating converters that are linked back-to-back, we are able to stabilize AC voltages and regulate the system frequency. A unique control method was created to optimize fuel economy, and it may be used to regulate the speed of the diesel engine. Using a double-loop control system, the DC-link voltage and battery current are regulated to keep power balanced and mitigate the effects of variable speed operation's slow dynamics. A combination of the perturbation and observation approach with the dynamic model of the DC-DC boost converter allows for efficient Maximum Power Point Tracking (MPPT). So that the Fuzzy Logic Controller's (FLC) unexpected shifts don't cause overshooting. This performance showcases the efficacy of coordinated control under varying loads and environmental circumstances, and it is executed using MATLAB/Simulink. Included in the package are off-grid hybrid systems, fuzzily-fed induction generators, coordinated control, tracking of maximum power points, battery energy storage, and fuzzy logic controllers.

I.INTRODUCTION

Due to its dependability, diesel generators (DG) have recently been the go-to option for providing power in remote parts of the globe. In this application, a 30-kW photovoltaic (PV) array is used to augment a 14.92 kw diesel generator (DG) that operates on a fixed-speed machine. Enhanced DE efficiency and fuel economy at light load are achieved by this, all while the noise and pollution produced by the DG are reduced. Although this approach is cost-effective, it exacerbates the issue of inadequate generator loading, leading to less efficient combustion and diesel engine efficiency (DE).

To examine this subject, we look at diesel engine applications that employ variable speed machine technology. Light loads are no match for the variable speed operation's DE efficiency and fuel economy. When there are variations in load or wind speed, or during transitions, this system's delayed dynamic reactivity becomes the major concern.

In order to address the concerns around a steady supply of electricity, it is necessary to control a hybrid off-grid system that includes a solar photovoltaic array and a variable-speed diesel engine. This allows the diesel engine's speed to be changed to match a predefined fuel consumption goal while still providing stable operation with ac voltages and system frequency management via the use of stator flux-oriented frame-based control and vector-based control for the back-to-back linked converters. An efficient method of control is developed. Integrating the de-de boost converter's dynamic model with the perturbation and observation approach also makes maximum power

point tracking (MPPT) straightforward and successful. All proportional-integral controllers use a back-calculation anti-windup approach to prevent overshoots during the abrupt transition. However, using an AWPl Controller will result in a system that has a slow reaction time and noticeable harmonic distortions. We use a Fuzzy Logic Controller in lieu of the AWPI Controller to circumvent these problems. As a result, the system responds quicker and errors are eliminated. You may use Matlab/Simlink to look at the simulation results.

II. PROPOSED SYSTEM

Figure 1 depicts a proposed hybrid off-grid system. The DE-driven variable speed DFIG's rotor terminals are connected to the PCC via back-to-back converters, while the stator terminals are linked to the PCC via the circuit breaker (CB). To disconnect the DFIG stator from the PCC while the DE is off and reconnect it when conditions are right, the CB is used. A common dc bus connects the SPA and BES, which are connected by dc-dc boost and dc-dc buck-boost converters, respectively. An ac dump load is connected to the dc side in order to stop BES from charging too much. With this OFF-grid setup, fuel economy is achieved at light loads and with the DE disabled, as the DG runs at variable speed based on the current load power demand (PL), maximum and minimum rated load power demand (Pn), power generated from the SPA (PSPA), and the battery energy storage system's state of charge (SoC%).

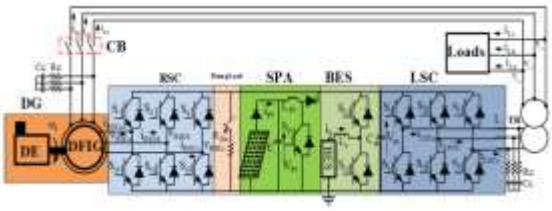

Fig. 1. Hybrid OFF-Grid system based on variable speed DG and SPA under study

III. CONTROL STRATAGY

A. Coordinated Control Strategy

The VSDG model and its coordinated control mechanism are shown in Figure 2. The DFIG, engine, speed regulator, and actuator are all part of this model. In this document, you may discover further information on the parameter design, mathematical models of the actuators and engines, and more. The DE speed is modulated by the actuator, while the precise fuel efficiency is provided by the governor. The ideal DE speed curve, together the coordinated control algorithm and the speed controller, make up the part that is responsible for managing the DE speed. In, we get into the specifics of DFIG control. The reference power (PDFIG$\prod$) is supplied via the coordinated control technique, which utilizes nine modes, as shown in Table I. In response to changes in load and ambient conditions, the DFIG may switch between super synchronous and sub synchronous modes of power generation.

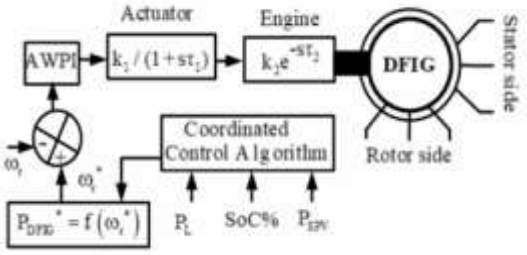

Fig. 2. DE model and its coordinated control

B. Control of RSC

The introduction of AWPI controllers improves the vector control system, as seen in Figure 3. Ensuring the DFIG gets the necessary magnetizing current and maintaining excellent performance across different DE speed circumstances are the two primary objectives of RSC control. In Fig. 1, we can see that BES stimulates the DFIG stator via LSC. The reference rotor speed ($c\prod$), the measured value (cZ), and the rotor speed error (Δcf) are sent into the proportional-integral controller (AWPI) with antiwindup feedback to determine the current along the quadrature axis of the RSC.

Industrial Engineering Journal
ISSN: 0970-2555
Volume : 53, Issue 9, September : 2024

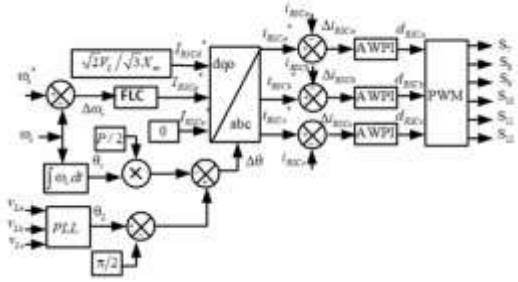

Fig. 3. Vector-oriented management for RSC

TABLE I

Operational Techniques of the Hybrid Off-Grid System

MODES	**Conditions**	**State of VSDG**	**State of BES**
1	SoC%=80%, $P_L \geq 0.8P_n$, $P_{SPA} \geq P_L$	Turned off	Stop charging
2	SoC%>80%, $P_L \geq 0.8P_n$, $P_{SPA} \geq P_L$	Turned off	Stop charging Activate dump load
3	50%≤SoC%≤80%, $P_L \geq 0.8$Pn, $P_{SPA} < P_L$	Turned off	BES Discharging
4	50%≤SoC%≤80%, P_L 0.8≥Pn, $P_{SPA} \geq P_L$	Turned off	BES charging
5	SoC%≤50%,0.3Pn $< P_L < 0.8P_n$, $P_{SPA} = P_L$	Sub-synchronous	charging BES
6	SoC%≤50%, 0.3Pn$< P_L <$ $0.8P_n$, PSPA=0	Super-synchronous	Fast charging BES
7	SoC%≤50%, 0.3Pn$< P_L$ $<0.8P_n$, $P_{SPA} < P_L$	Super-synchronous	Fast charging BES
8	50%≤SoC%<80%, 0.3Pn$< P_L$, $P_{SPA} \geq 0$	Sub-synchronous	Charging BES
9	SoC% ≥80%, 0.3Pn$< P_L$ <0.8Pn, PSPA ≤PL	Turned off	Stop charging BES

$((I^*_{RSCq})$ as

$$\left(I^*_{RSC(abc)}\right) = T_{dq0}(\Delta\theta)^{-1}[I^*_{RSC(dq0)}] \quad (1)$$

where $T_{dq0}(\Delta\theta)^{-1}$ represents the inverse Park's transformation and expressed as

$$\begin{bmatrix} \cos(\Delta\theta) & \sin(\Delta\theta) & 1 \\ \cos(\Delta\theta - 2\pi/3) & \sin(\Delta\theta - 2\pi/3) & 1 \\ \cos(\Delta\theta + 2\pi/3) & \sin(\Delta\theta + 2\pi/3 & 1 \end{bmatrix} \quad (2)$$

where $\Delta\theta$ represents rotor transformation angle, calculated as

$$\Delta\theta = \left(\theta_s - \frac{\pi}{2}\right) - \left(\frac{P}{2}\right)\theta_r \quad (3)$$

where P, θ_r, and $\theta_s$represent number of DFIG poles, rotor, and stator angles, respectively. θ_s is obtained using a phased locked loop whereas, θ_s is obtained by integrating the rotor speed

$$\theta_r = \int_0^t \omega_r dt \quad (4)$$

The estimated reference rotor currents are compared with sensed RSC currents to get duty cycles (i_{RSCa}, i_{RSCb}, and i_{RSCc}) as

$$\begin{cases} d_{RSCa} = k_{p2}\Delta i_{RSCa} + \left(k_{i2} - \dfrac{e_2}{Ta_2}\right)\int_0^t \Delta i_{RSCa}dt \\ d_{RSCb} = k_{p2}\Delta i_{RSCb} + \left(k_{i2} - \dfrac{e_2}{Ta_2}\right)\int_0^t \Delta i_{RSCb}dt \\ d_{RSCc} = k_{p2}\Delta i_{RSCc} + \left(k_{i2} - \dfrac{e_2}{Ta_2}\right)\int_0^t \Delta i_{RSCc}dt \end{cases} \quad (5)$$

Industrial Engineering Journal
ISSN: 0970-2555
Volume : 53, Issue 9, September : 2024

where k_{p2}, k_{i2}, e_2, and Ta_2 denote the PI controller gains of the inner loop, the error between the saturated and unsaturated control signals, and the antiwindup gain, respectively. The obtained duty cycles are fed to PWM controller to get switching signal for (S_7–S_{12}).

Fig. 4 shows developed control algorithm of dc–dc boost converter. To achieve high performance from SPA under solar irradiation change, the improved P&O technique given in [21], and dynamic model of the dc–dc boost converter are combined. The reference PV current (I_{mPV}) is estimated using the P&O technique. The measured SPA current (I_{PV}) is compared with $I_{mPV}$and the error is fed to the PI current controller with antiwindup feedback as

$$u_i = k_{p3}(I_{mPV} - I_{PV}) + \left(k_{i3} - \frac{e_3}{T_{a3}}\right)\int_0^t (I_{mPV} - I_{PV})dt \quad (6)$$

where k_{p3}, k_{i3}, e_3, and T_{a3} denote proportional and integral gains of the controller, the error between saturated and unsaturated control signals, and the antiwindup gain, respectively. The duty cycle (d) is obtained using output of PI controller (u_i) and dynamic model of dc–dc boost converter [22] as

$$d = 1 + \frac{u_i - V_{PV}}{V_{dc}} \quad (7)$$

The obtained duty cycle is fed to the PWM controller to get the switching signal for the switch S1.

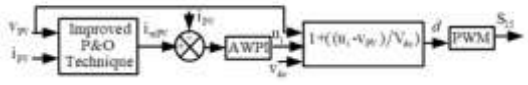

Fig.4. Control strategy for DC–DC boost converter

D. Control of DC–DC Buck–Boost Converter

Fig. 5 demonstrates developed control algorithm for dc–dc buck–boost converter. To balance power in OFF-grid system, to compensate SPA intermittency, and to ensure an uninterruptible power to connected load, especially during increase or decrease of VSDG speed, transition between different operating modes of DFIG, double-loop control is developed. Reference BES current (i^*_{bat}) is obtained as

$$i^*_{bat} = k_{p4}(V^*_{dc} - V_{dc}) + \left(k_{i4} - \frac{e_4}{T_{a4}}\right)\int_0^t (V^*_{dc} - V_{dc})dt \quad (8)$$

where kp4, ki4, e4 and Ta4, Vdc, and Vdc∗ denote the proportional and integral gains of the outer control loop, the error between the saturated and unsaturated control signal, and the antiwindup gain, dc-link voltage, and its reference, respectively. The measured BES current (i_{bat}) is compared with its reference i^*_{bat} and the BES current error is fed to PI controller with antiwindup feedback to get the duty cycle (d1) to generate the switching signal for S13 and S14.

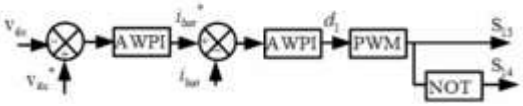

Fig.5.Control strategy for dc–dc buck–boost converter

D. Control of LSC

In Fig. 6, the control algorithm for the load side converter (LSC), is presented. To inject power into PCC and to maintain a constant ac voltage and system frequency, stator fluxoriented frame-based control is employed [23]. The reference d-component of the stator current (i^*_{sd}) is estimated as

$$i^*_{sd} = k_{p5}\Delta V_{PL} + \left(k_{i5} - \frac{e_5}{T_{a5}}\right)\int_0^t \Delta V_{PL}\, dt \quad (9)$$

where k_{p5}, k_{i5}, e_5, T_{a5} and ΔV_{PL} denote proportional and integral gains of controller, the error between the saturated and unsaturated control signals, antiwindup gain, and error in PCC voltage, obtained by comparing reference amplitude of PCC voltage given in [12], and its measured value (VPL), as

$$V_{PL} = \sqrt{\left(\frac{2}{3}\right)(V_{La}^2 + V_{Lb}^2 + V_{Lc}^2)} \quad (10)$$

where V_{La}, V_{Lb}, and V_{Lc} represent the measured PCC voltages.

The stator current in q-axis (i^*_{sq}) is obtained as

$$i^*_{sq} = -\left(\frac{L_m}{L_s}\right) i_{RSCq} \quad (11)$$

Where L_m, L_s, and i_{RSCq} are mutual and stator inductances and RSC current in q-axis. The system

Industrial Engineering Journal
ISSN: 0970-2555
Volume : 53, Issue 9, September : 2024

frequency regulation is realized by forcing LSC to operate at 60 Hz as

$$\theta_s = 2\pi f_s t \quad (12)$$

where t and fs represent sampling time and the stator frequency, which is equal to 60 Hz. The reference currents of the stator (isa∗, isb∗, and isc∗) are obtained using inverse Park Transformation matrix as [20]

$$[i^*_{eabc}] = T_{dq0}(\theta_s)^{-1}[I^*_{sdq0}] \quad (13)$$

where Tdqo (θs) −1 represents inverse Park's transformation. Measured stator currents are compared with references and errors in stator currents are fed to PI current controllers with antiwindup feedback for inner control loops to get duty cycles (dsa, dsb, and dsc) as

$$\begin{cases} d_{Sa} = k_{p6}\Delta i_{Sa} + \left(k_{i6} - \frac{e_6}{Ta_6}\right) \int_0^t \Delta i_{Sa} dt \\ d_{Sb} = k_{p6}\Delta i_{Sb} + \left(k_{i6} - \frac{e_6}{Ta_6}\right) \int_0^t \Delta i_{Sb} dt \\ d_{Sc} = k_{p6}\Delta i_{Sc} + \left(k_{i6} - \frac{e_6}{Ta_6}\right) \int_0^t \Delta i_{Sc} dt \end{cases} \quad (14)$$

where k_{p6}, k_{i6}, e_6, and e_6 denote the PI, controller gains of inner control loops, the error between the saturated and unsaturated control signal, and antiwindup gain, respectively. The obtained duty cycles are fed to the PWM controller to get the switching signal for (S_1–S_6).).

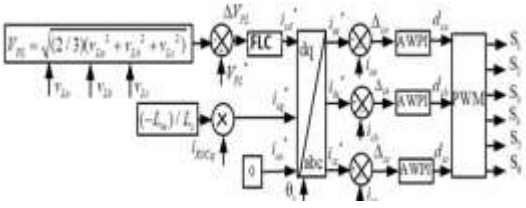

Fig.6. Control algorithm for LSC

The fuzzy approach consists of three primary phases. Level one, input; level two, processing and stages Next, we have the Output Stage. The error signal is fed to the Fuzzy controller and used as feedback. In the processing step, membership and truth values are used to decrease the signal-to-noise ratio. By eliminating noise from the output volume, the output stage may now be regulated and set to a certain value. The fuzzy-based logic controller's four-step setup: First, never stop moving. The source of law 3) The inference procedure fourthly, untangling. The PI controller has surpassed all others in industrial settings due to its basic form, low cost, and ease of manufacture. Despite these benefits, PI controllers fail miserably when dealing with things that are very non-linear and unpredictable. This makes developing a fuzzy logic controller more easier while yet retaining the advantages of a PI-style control system. The control output is given by

$$K_p\Delta u_f + k_i \int e\, dt \quad (15)$$

where kp and ki are the same as in the basic PI controller and stand for the FLC output. The look of fuzzy Pairing fuzzy variables with input variables is what fluzzification is all about. There is a distinct membership function for every fuszified variable. To keep the inputs and outputs afloat, as shown in Figure 5, three sets of fluids are utilized: P for positive, Z for zero, and N for negative. Inputs to the fuse controller include both the original and derivative errors.

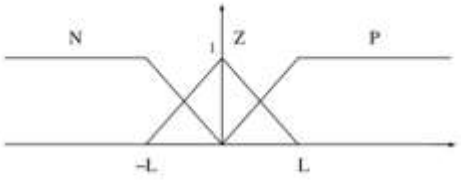

Figure 7. Membership functions for fuzzy controller

IV. PROPOSED FUZZY LOGIC CONTROLLER

$$\mu_p(x_i) = \begin{cases} 0 & xi < 0 \\ \frac{xi}{L} & 0 \le xi \le L \\ 1 & xi > L \end{cases} \quad (16)$$

Industrial Engineering Journal
ISSN: 0970-2555
Volume : 53, Issue 9, September : 2024

Where xi marks the controller fuzzy inputs. The adverse member feature is similarly

$$\mu_N(x_i) = \begin{cases} 1 & xi < -L \\ \frac{-xi}{L} & -L \le xi \le 0 \\ 0 & xi > 0 \end{cases} \quad (17)$$

And the membership feature is zero set:

$$\mu_Z(x_i) = \begin{cases} 0 & xi < -L \\ \frac{xi+L}{L} & -L \le xi \le 0 \\ \frac{-xi+L}{L} & 0 < xi \le L \\ 0 & x_i > L \end{cases} \quad (18)$$

Inference

The variables that can be altered provide the basis for control decision-making. Details act as guides and inform production decisions. In Table 1 you can see the foundational rules of the controller. Using the min-max inference, we can find out how much of a member the output variables are. The image. 2. It was suggested to use a fuzzy controller. Make an effort.

Fuzzy controller table 1 Rule Base

$\dot{e}[k]$	$e[k]$ $\Delta u_f[k]$		
	N	Z	P
N	N	N	Z
Z	N	Z	P
P	Z	P	P

Defuzzification

In numerical output, the output variables for the fuzzy inference method should be transformed. Use Zadeh operating rules and general defuzzifier for fuzzy controller output:

$$\Delta u_f(k) = \frac{\sum_{i=1}^{9} \mu c(\mu f)\mu f}{\sum_{i=1}^{9} \mu c\,(\mu f)} \quad (19)$$

Fuzzy logic is one approach to real-time governance. Identified by considering many factors and using a resolution method based on multiple rules. More and more people have started using Fuzzy MPPT in the last decade. Among the several advantages of fuzzy logic controllers are their tolerance for non-linearity, ability to operate with defective inputs, and lack of necessity for an accurate mathematical model. Figure 3 displays the Fuzzy MPPT model in Simulink.Two inputs and one output characterize it. The error (E) and the change of error (CE) are two variables that FLC takes as input. D stands for duty cycle output variable. As a result, tracking performance under linear and nonlinear loads may be improved using fuzzy control algorithms in comparison to conventional methods. Nonlinear control is a good fit for fuzzy logic since it doesn't depend on complex mathematical formulae. Among several other things, the structure of the membership functions in the rule base determines how an FLC will perform.

To construct our membership functions and rule base, we use the Fuzzy Logic Tool Box in MATLAB. Here we can see the error membership function from a graphical standpoint in Figure.Fuzzy logic causes input errors, as seen in Figure 6.7. The error's evolution is shown by the picture.A fuzzy logic controller's duty cycle is shown in Figure 9.0, whereas Figure 8 shows the same thing.

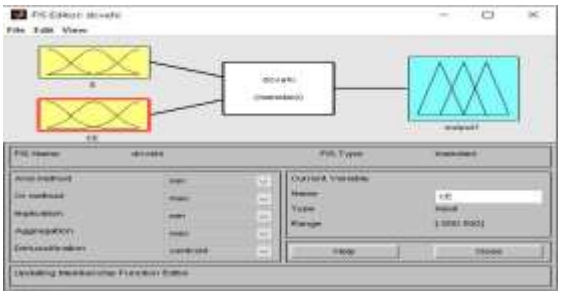

Figure.8 Fuzzy logic Implementation in Simulation

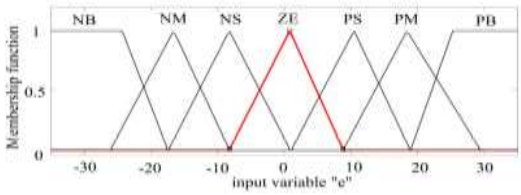

Figure.9 Fuzzy logic input Error (E)

Industrial Engineering Journal
ISSN: 0970-2555
Volume : 53, Issue 9, September : 2024

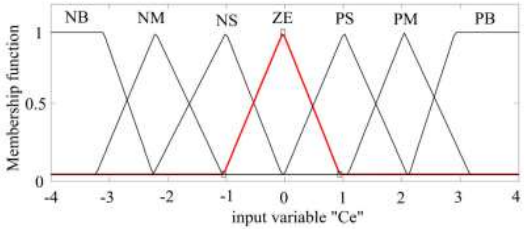

Figure.10 Fuzzy logic input change of Error (CE)

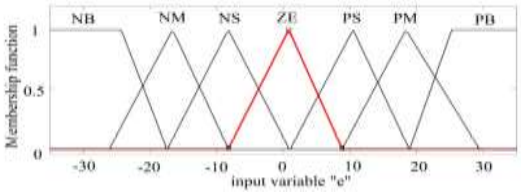

V. SIMULATION RESULTS

A) EXISTING RESULTS

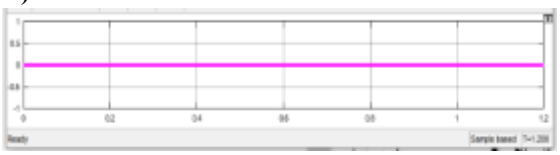

Isa(A)

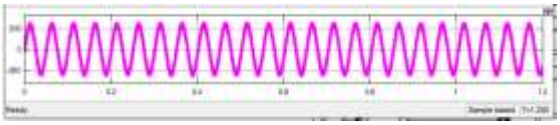

Vla(V)

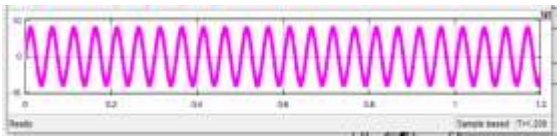

Ila(A)

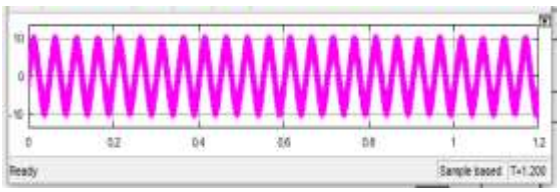

ILSC (A)

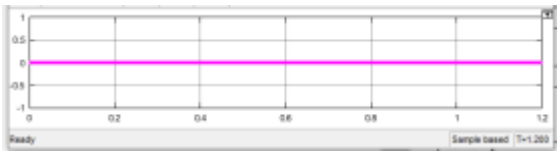

IRSC (A)

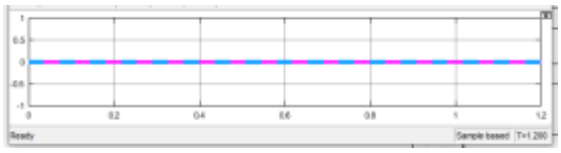

WR &WR*

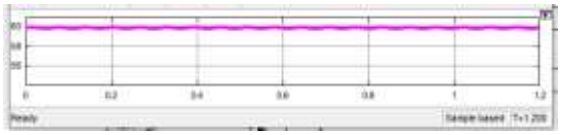

Fs(Hz)

(a)

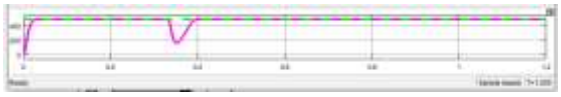

Vdc &Vdc*

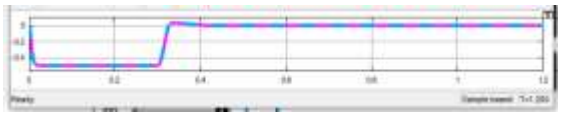

Ib & Ib*

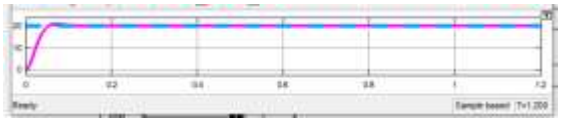

IPV & IPV*

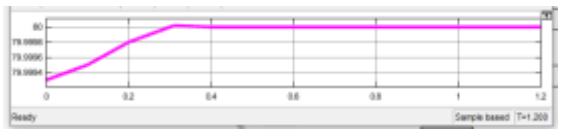

SOC %

(b)

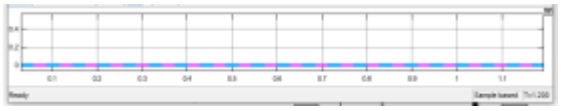

Ps & Qs

PRSC & QRSC

Industrial Engineering Journal
ISSN: 0970-2555
Volume : 53, Issue 9, September : 2024

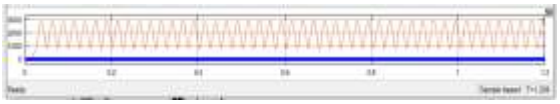

PL & QL

PLSC & QLSC

PPV

PB

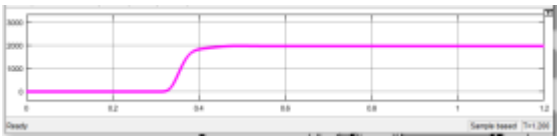

PDm

(c)

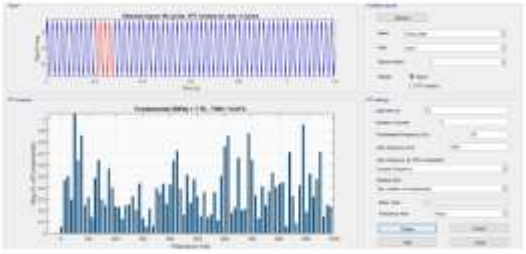

(d)

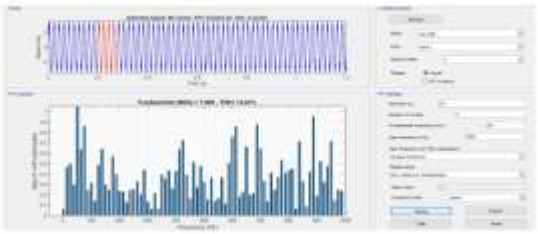

(e)

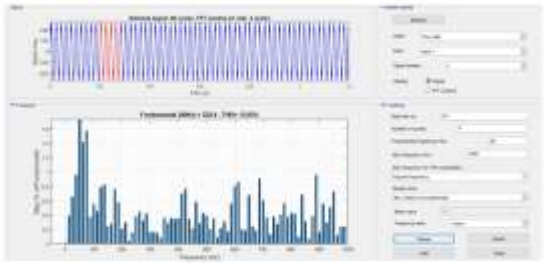

(f)

Fig. 12. Dynamic performance at (a)ac side, (b)dc side, (c)power flow when the system operates in Modes 1 and 2, (d) Inverter Current THD (e) Load Current THD and (f) Load Voltage THD

isa

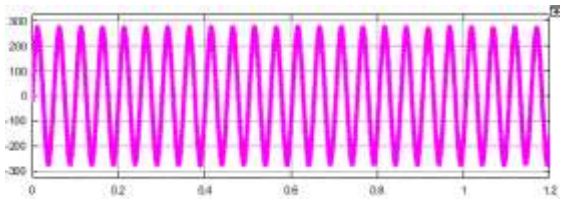

VLa

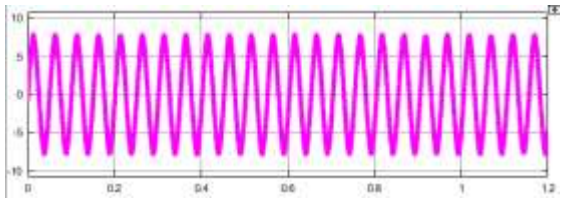

ILa

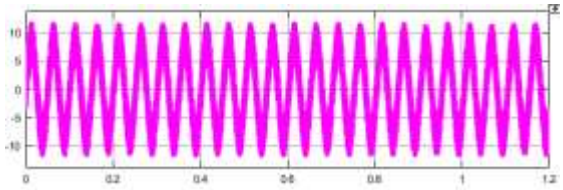

ILSCa

Industrial Engineering Journal
ISSN: 0970-2555
Volume : 53, Issue 9, September : 2024

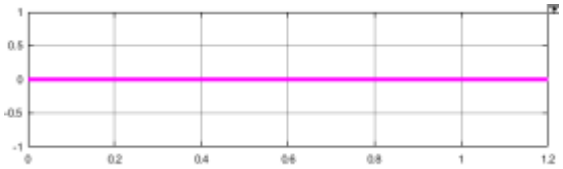

IRSCa

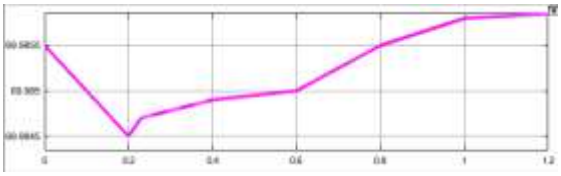

SOC

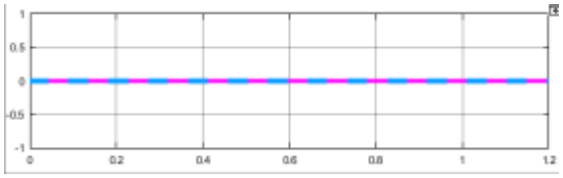

Wr & W

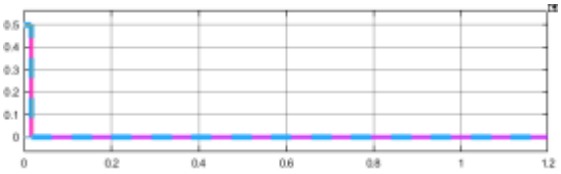

VS & IS

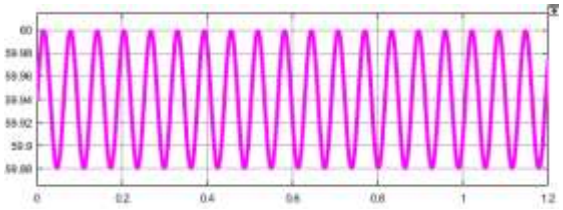

Fs

(a)

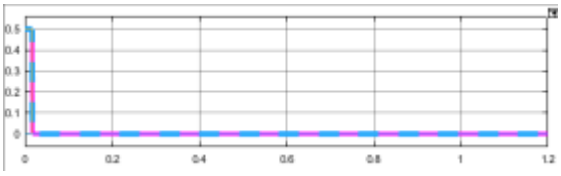

VRSC & IRSC

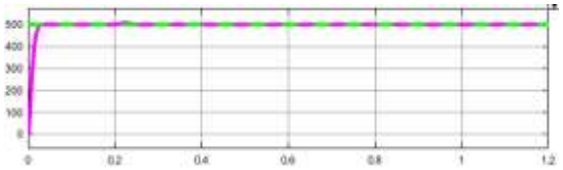

Vdc & VdcR

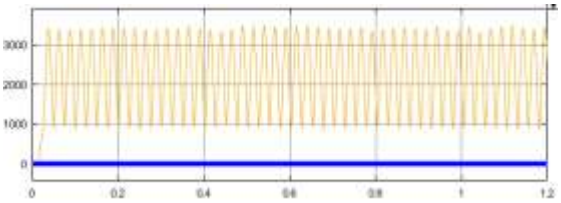

VL & IL

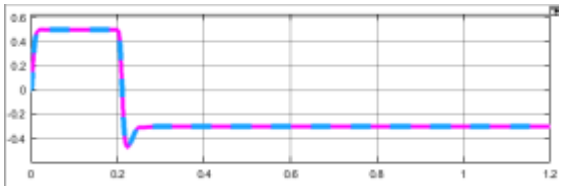

IB & IBR

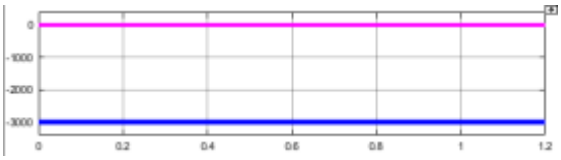

VLSC & ILSC

(b)

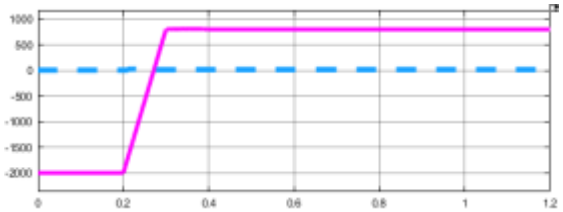

IPV & IPVR

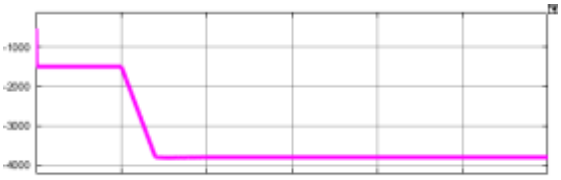

PPV

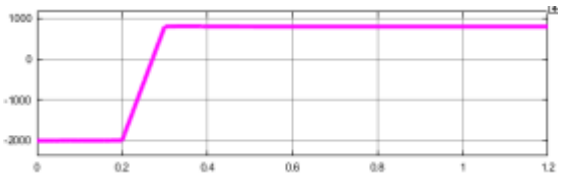

Industrial Engineering Journal
ISSN: 0970-2555
Volume : 53, Issue 9, September : 2024

PB

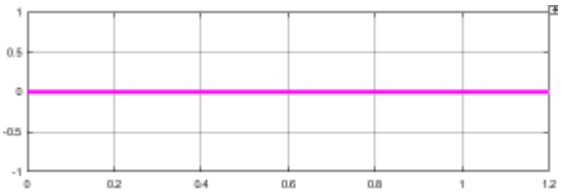

PDm

(c)

(d)

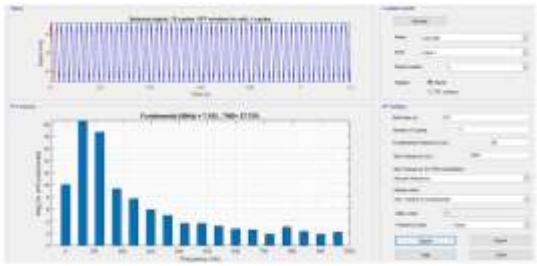

(e)

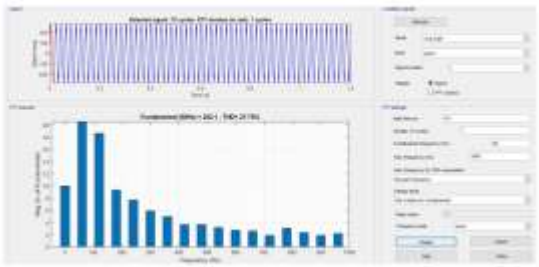

(f)

Fig. 13. Dynamic performance at (a)ac side, (b)dc side,(c)power flow when the system operates in Modes 3 and 4, (d) Inverter Current THD (e) Load Current THD and (f) Load Voltage THD

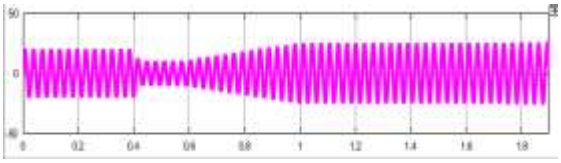

isa

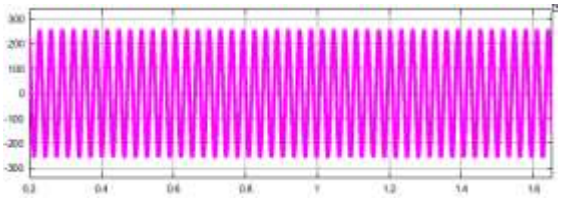

VLa

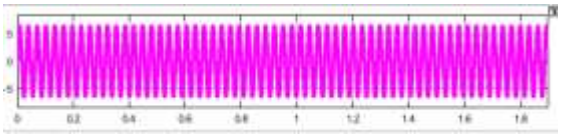

ILa

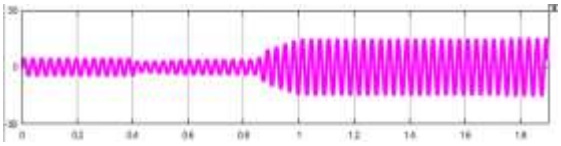

ILSCa

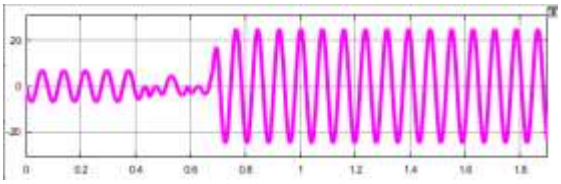

IRSCa

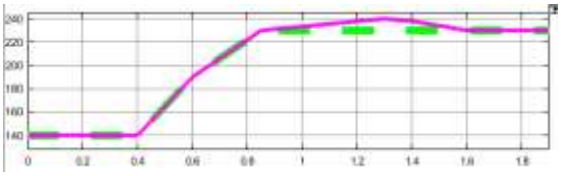

Wr & W

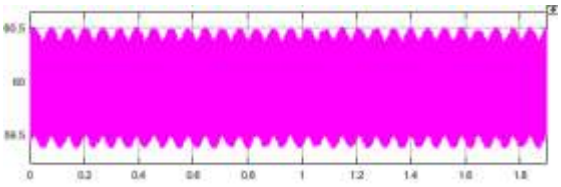

Fs

(a)

Industrial Engineering Journal
ISSN: 0970-2555
Volume : 53, Issue 9, September : 2024

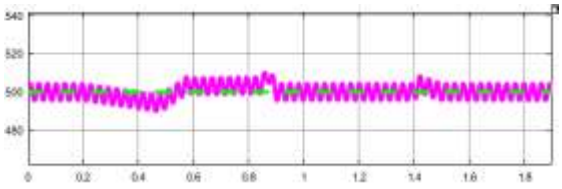

Vdc & VdcR

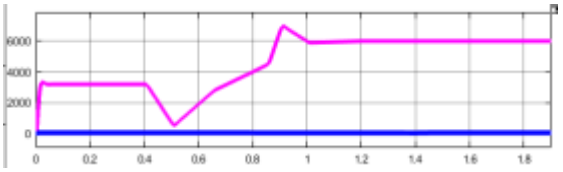

VLSC & ILSC

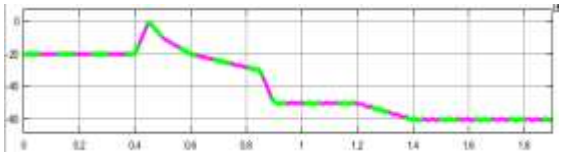

IB & IBR

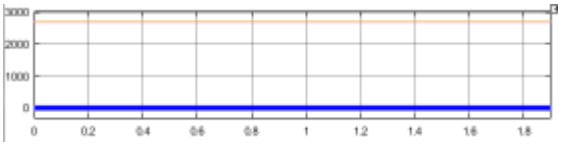

VL & IL

(b)

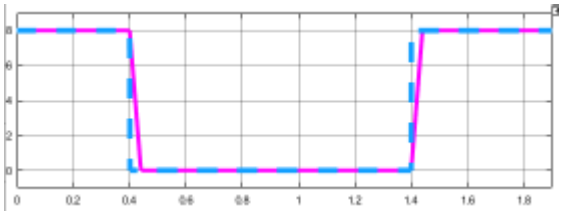

IPV & IPVR

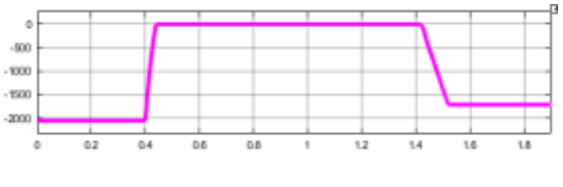

PPV

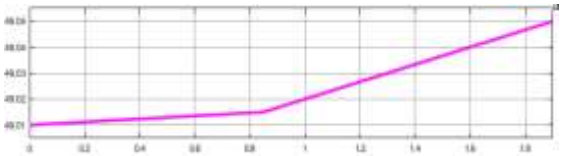

SOC

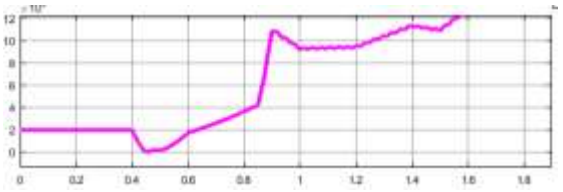

PB

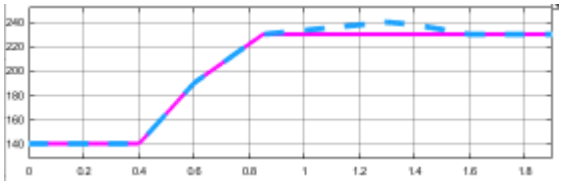

Wr & W

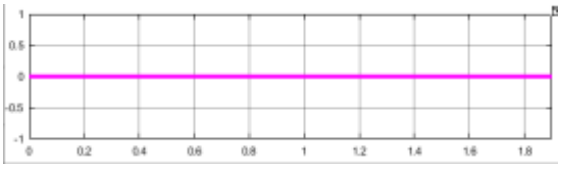

PDm

(c)

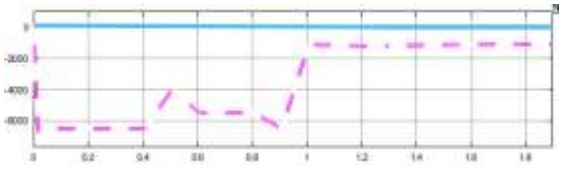

VS & IS

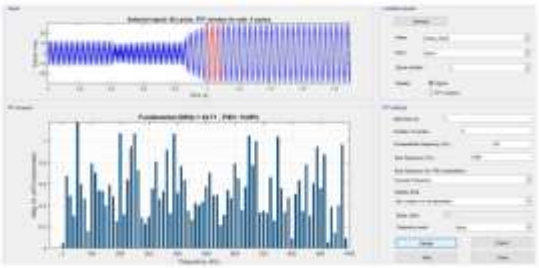

(d)

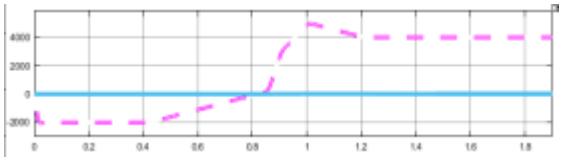

VRSC& IRSC

Industrial Engineering Journal
ISSN: 0970-2555
Volume : 53, Issue 9, September : 2024

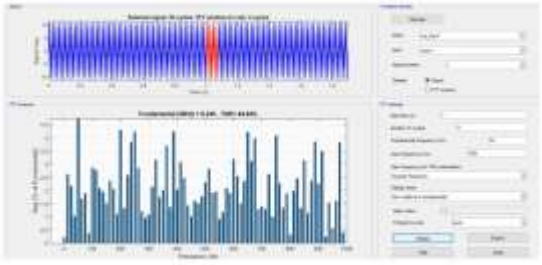

(e)

(f)

Fig. 14. Dynamic performance at (a)ac side, (b) dc side, (c) power flow when the OFF-grid system operates in modes 5, 6, and 7, (d) Inverter Current THD (e) Load Current THD and (f) Load Voltage THD

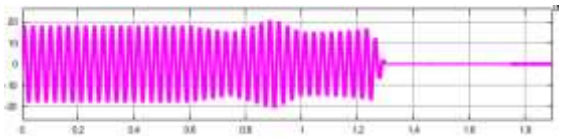

isa

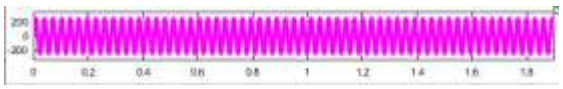

VLa

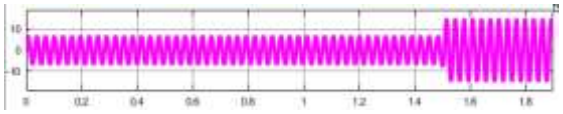

ILa

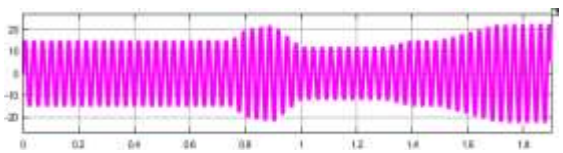

ILSCa

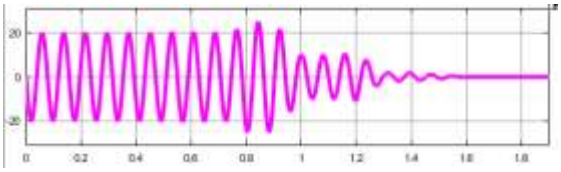

IRSCa

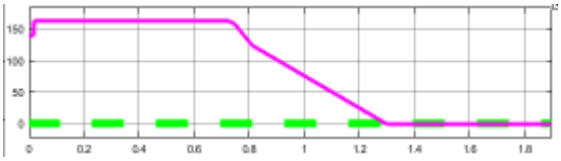

Wr & W

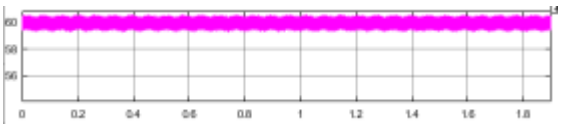

Fs

(a)

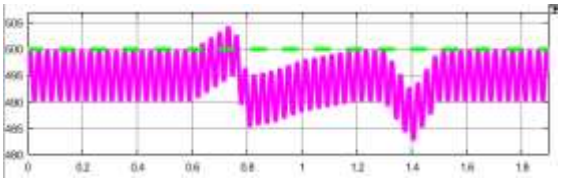

Vdc & VdcR

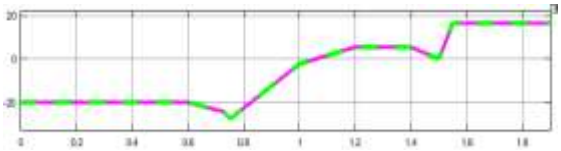

IB & IBR

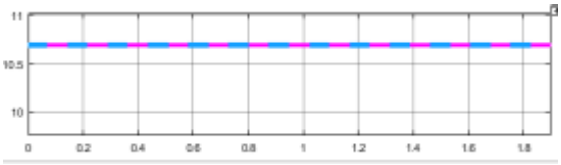

IPV & PVR

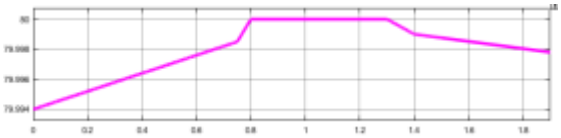

SOC

Industrial Engineering Journal
ISSN: 0970-2555
Volume : 53, Issue 9, September : 2024

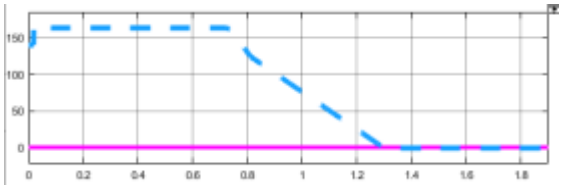

Wr & W

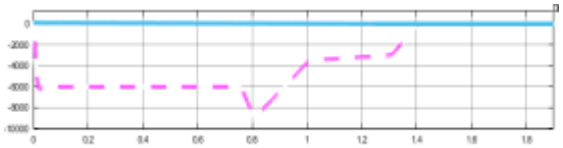

VS & IS

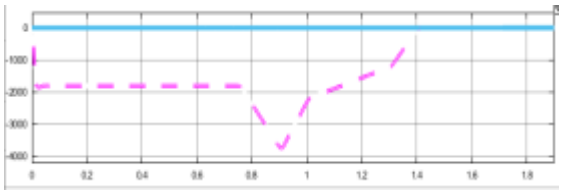

VRSC & IRSC

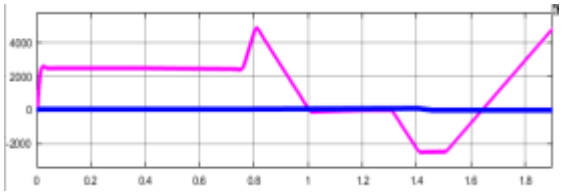

VLSC & ILSC

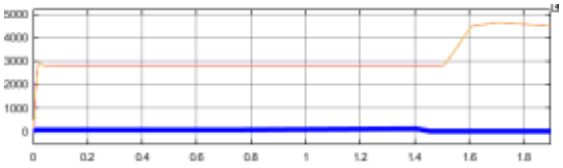

VL & IL

(b)

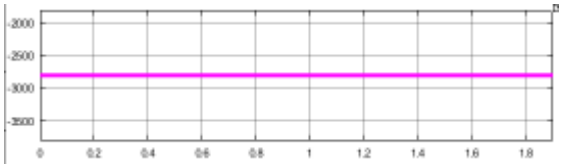

PPV

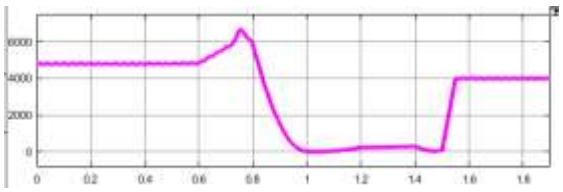

PB

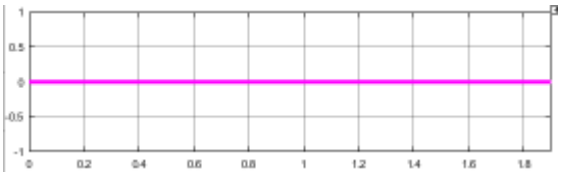

PDm

(c)

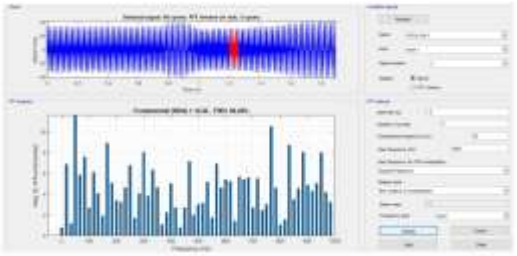

(d)

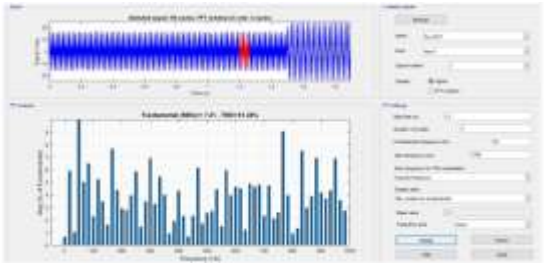

(e)

(f)

Fig.15 Dynamic performance at (a) ac side, (b) dc side, (c) power flow when the system operates in Modes 8 and 9, and at sudden load increment, (d) Inverter Current THD (e) Load Current THD and (f) Load Voltage THD

B) EXTENSION RESULTS

Industrial Engineering Journal
ISSN: 0970-2555
Volume : 53, Issue 9, September : 2024

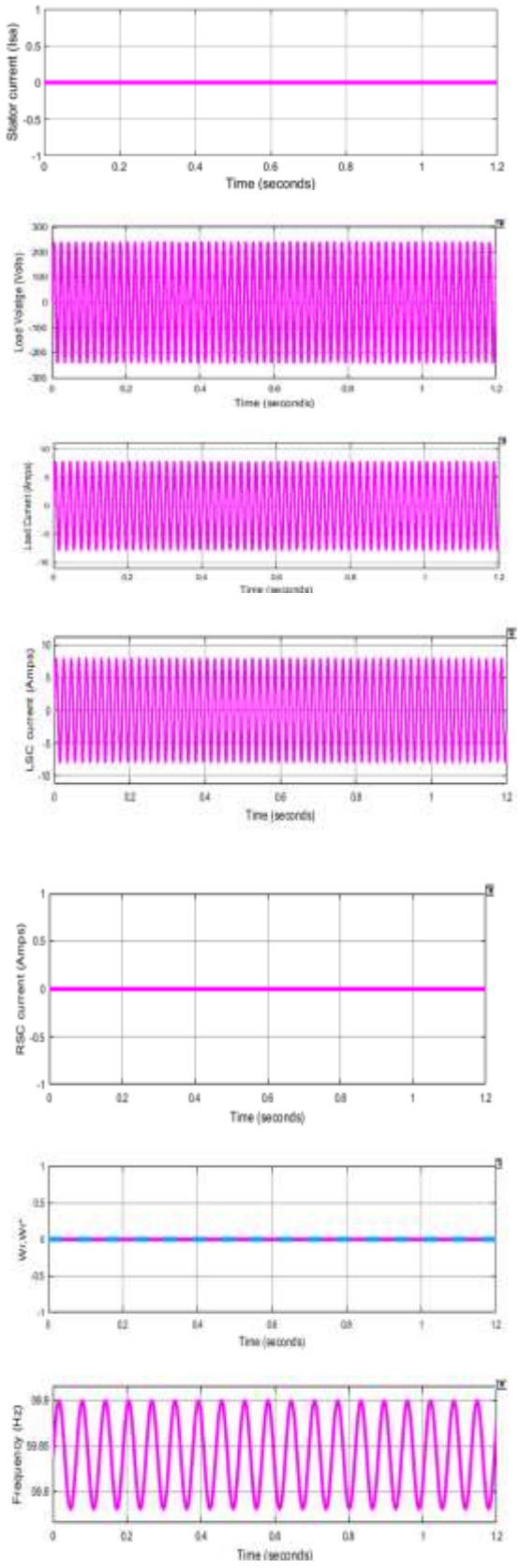

(a)

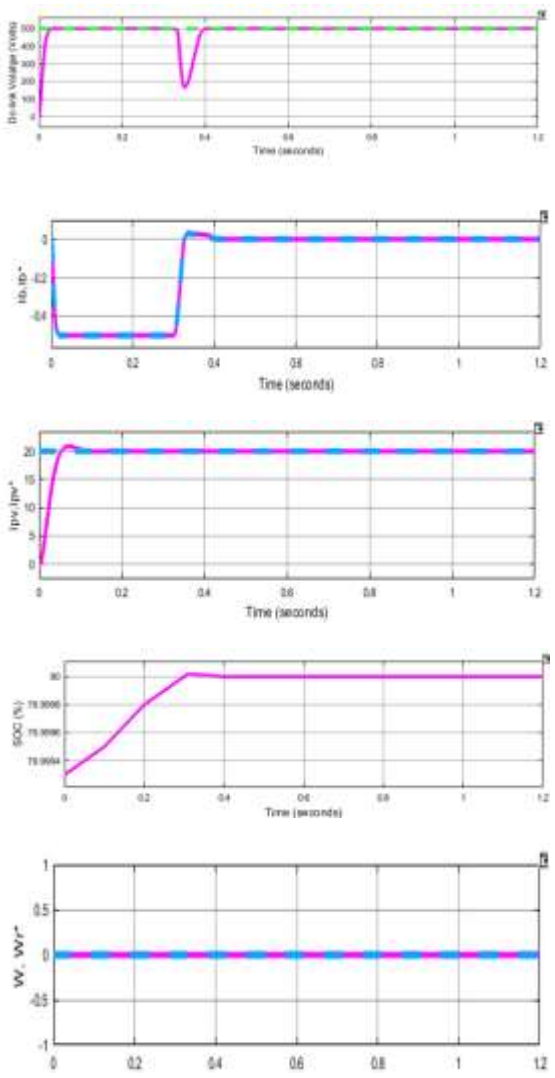

(b)

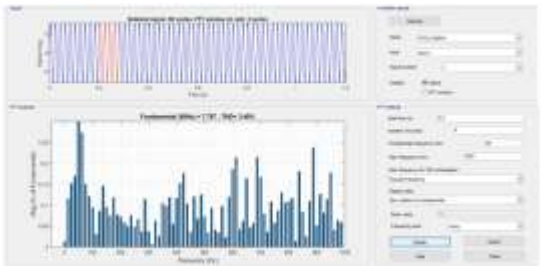

(c)

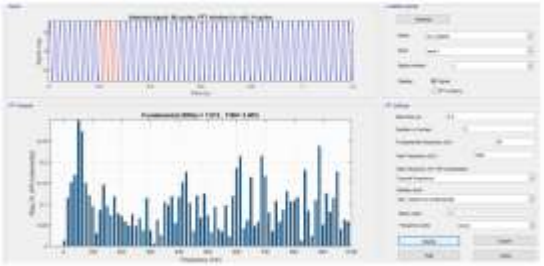

Industrial Engineering Journal
ISSN: 0970-2555
Volume : 53, Issue 9, September : 2024

(d)

(e)

Fig. 12. Dynamic performance at (a)ac side, (b)dc side, (c) Inverter Current THD (d) Load Current THD and (e) Load Voltage THD

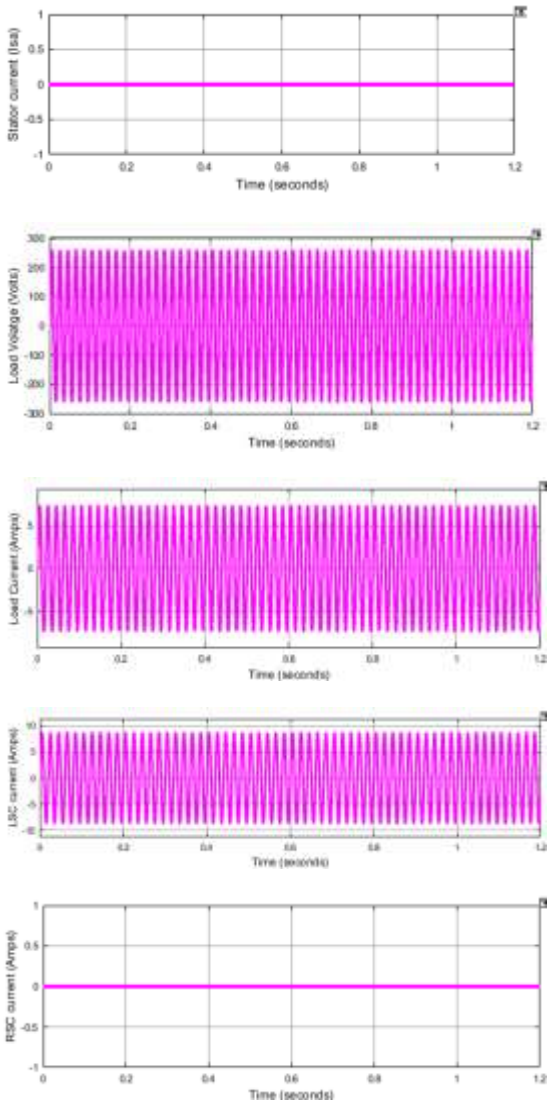

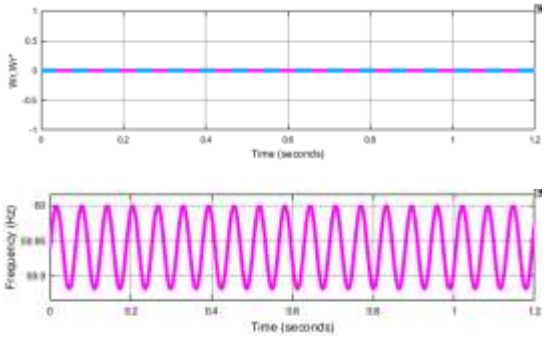

(a)

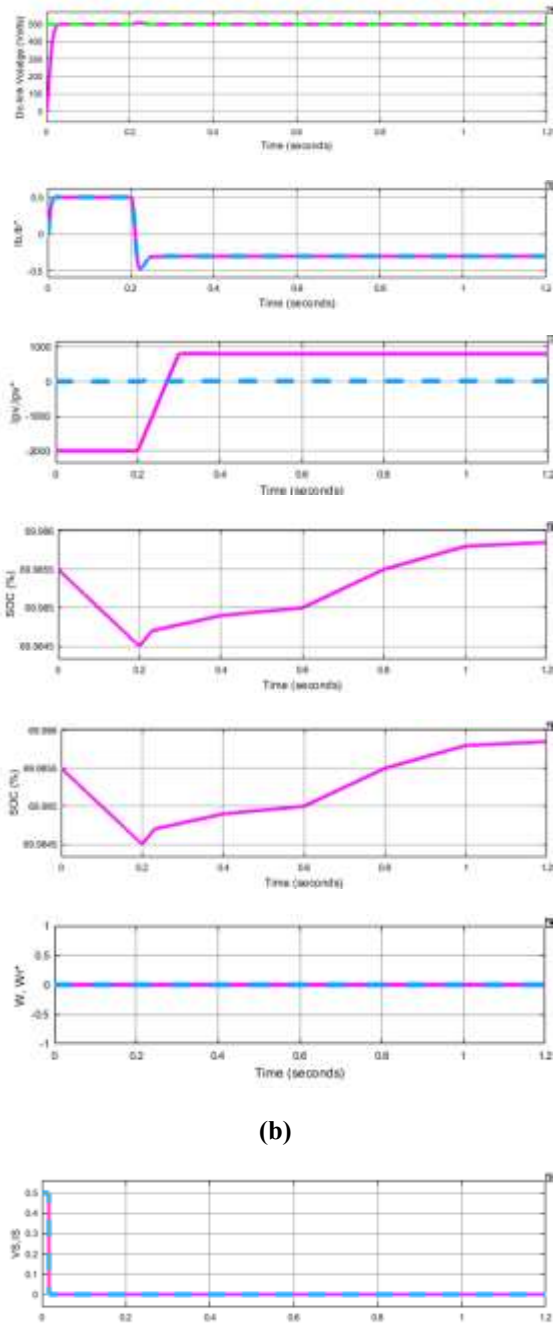

(b)

Industrial Engineering Journal
ISSN: 0970-2555
Volume : 53, Issue 9, September : 2024

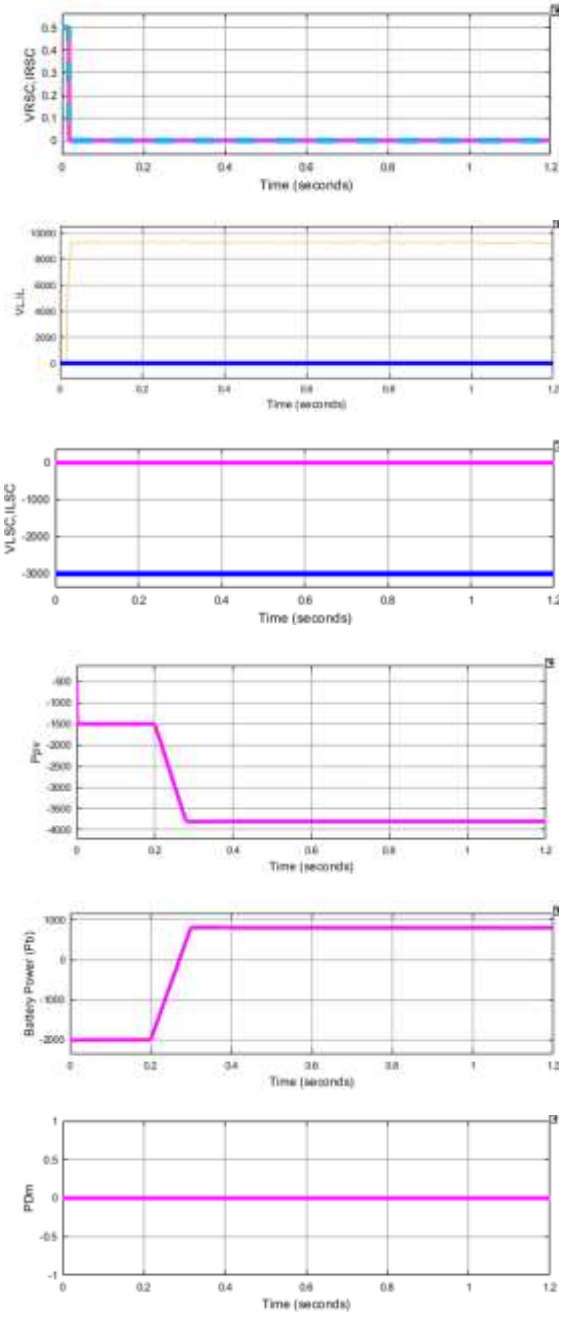

(c)

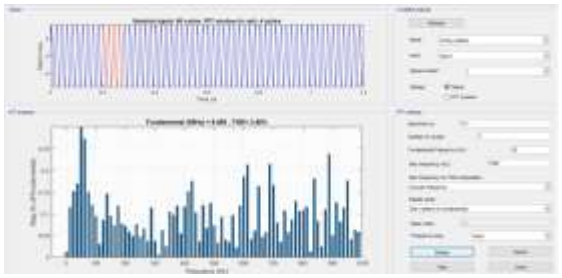

(d)

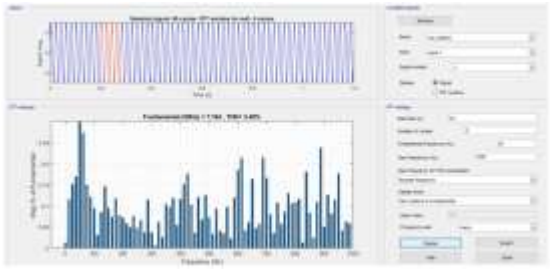

(e)

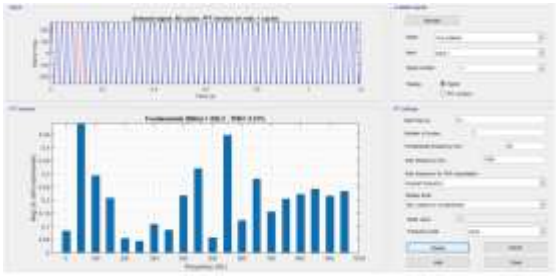

(f)

Fig. 17. Dynamic performance at (a)ac side, (b)dc side,(c)power flow when the system operates in Modes 3 and 4, (d) Inverter Current THD (e) Load Current THD and (f) Load Voltage THD

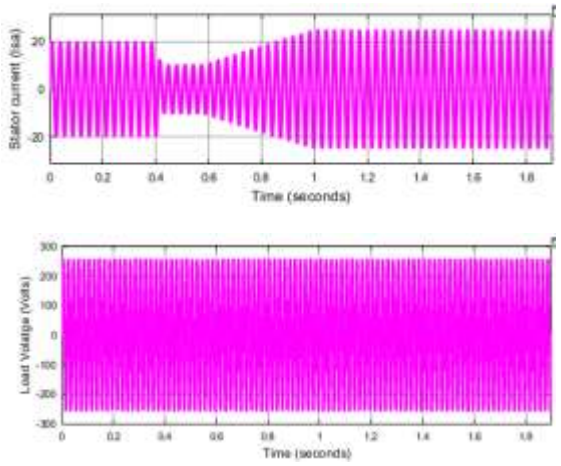

Industrial Engineering Journal
ISSN: 0970-2555
Volume : 53, Issue 9, September : 2024

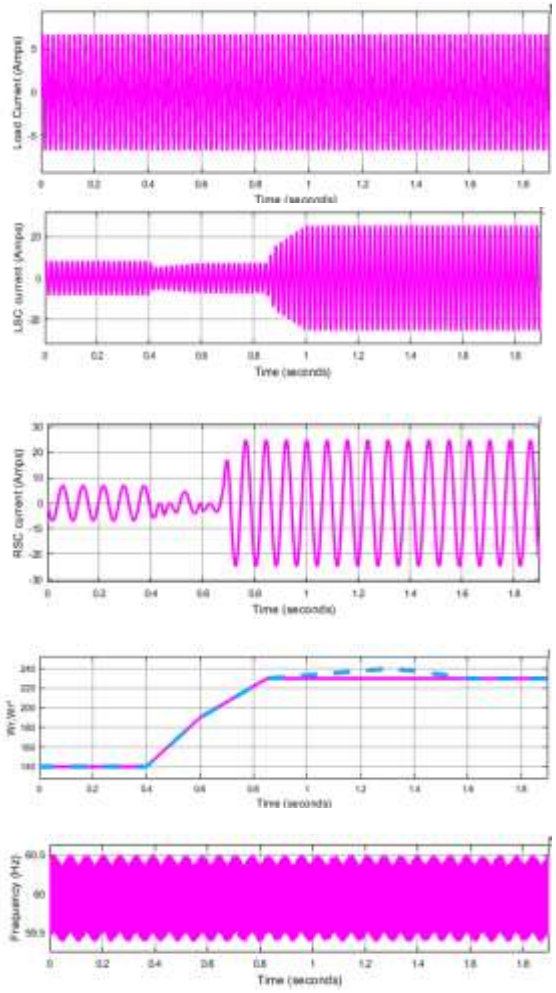

(a)

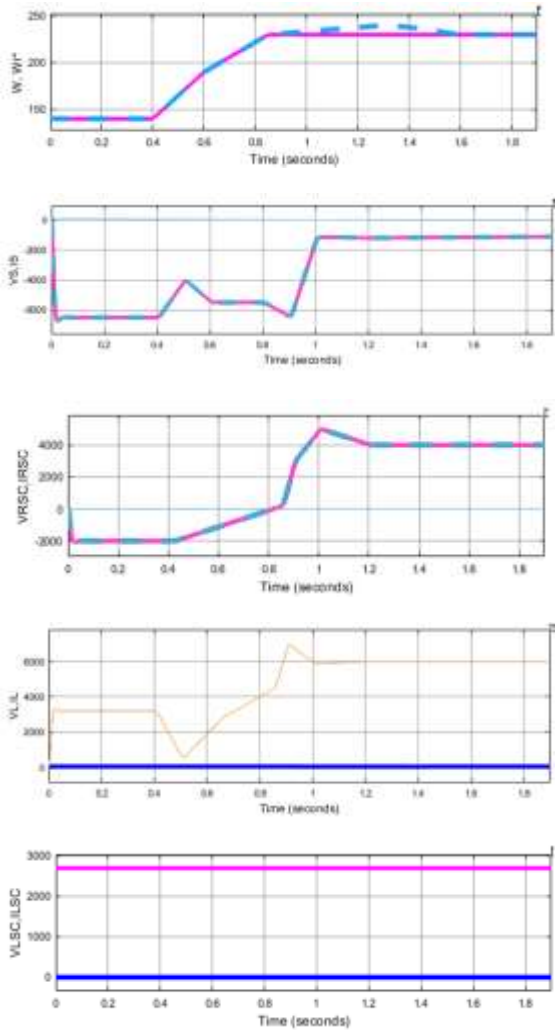

(b)

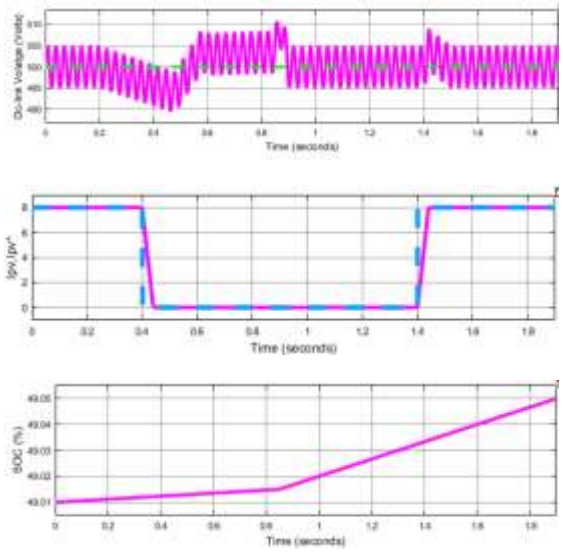

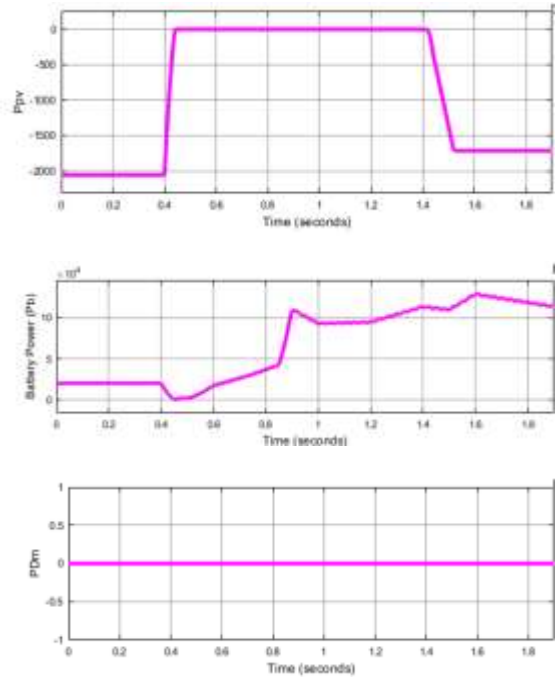

Industrial Engineering Journal
ISSN: 0970-2555
Volume : 53, Issue 9, September : 2024

(c)

(d)

(e)

(f)

Fig. 17. Dynamic performance at (a)ac side, (b) dc side, (c) power flow when the OFF-grid system operates in modes 5, 6, and 7, (d) Inverter Current THD (e) Load Current THD and (f) Load Voltage THD

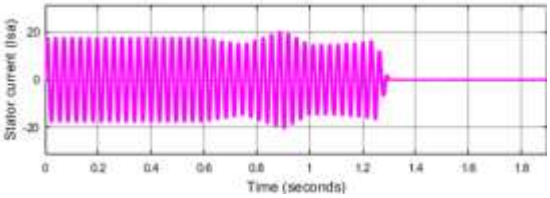

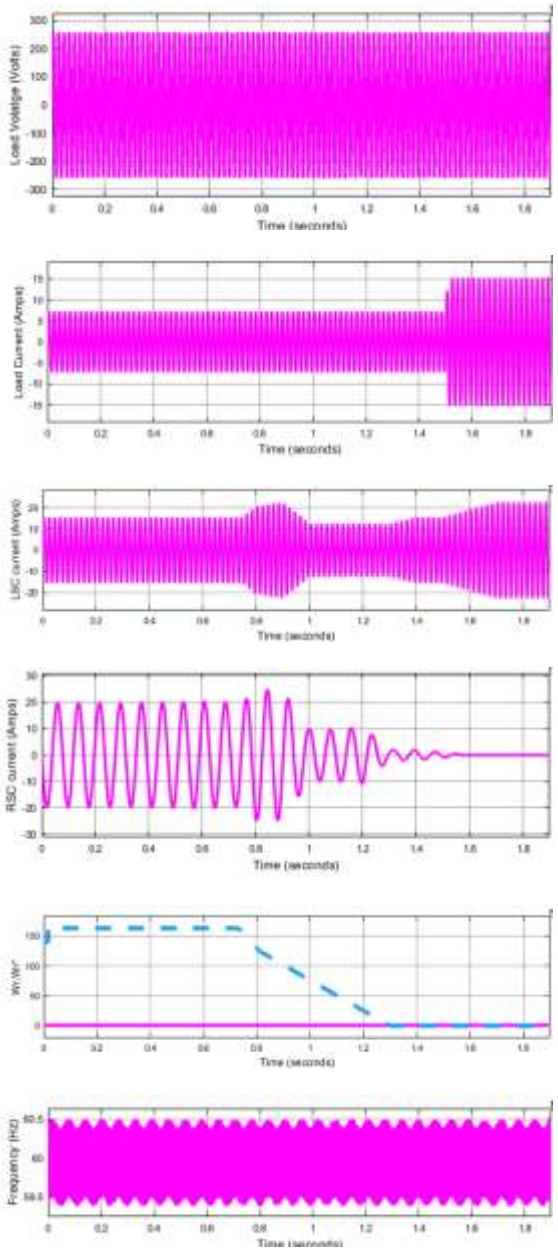

(a)

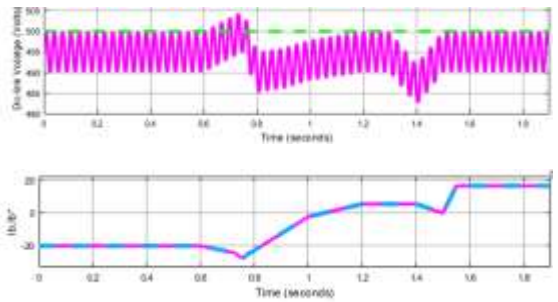

Industrial Engineering Journal
ISSN: 0970-2555
Volume : 53, Issue 9, September : 2024

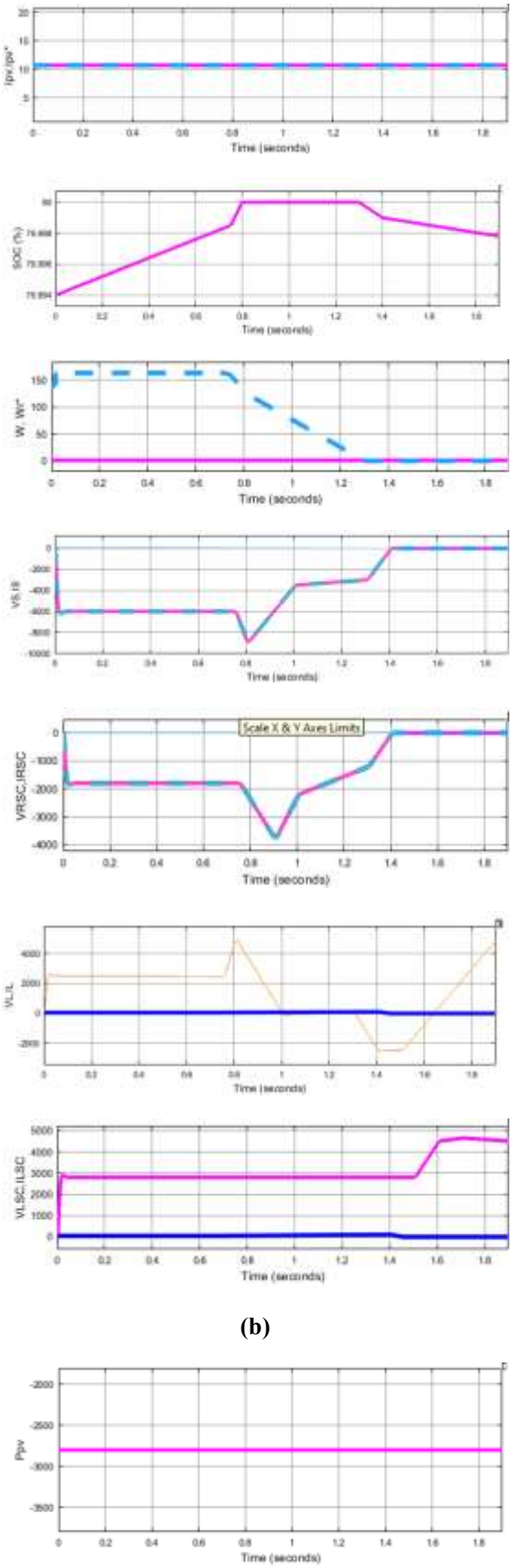

(b)

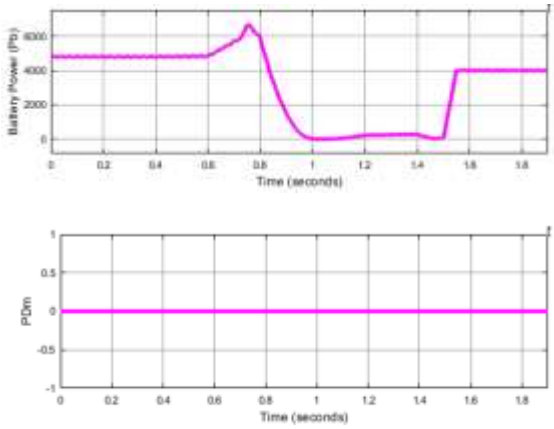

(c)

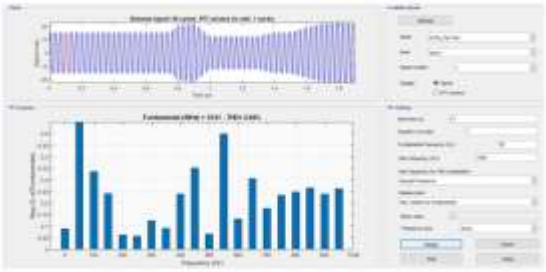

(d)

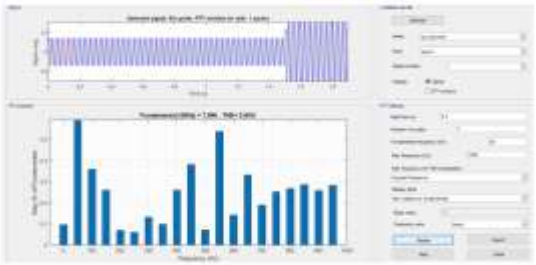

(e)

(f)

Fig.19 Dynamic performance at (a) ac side, (b) dc side, (c) power flow when the system operates in Modes 8 and 9, and at sudden load increment, (d) Inverter Current THD (e) Load Current THD and (f) Load Voltage THD

THD COMPARISION TABLE-1

THD COMPARISION TABLE-1

Case-1 System operates in modes 1 and 2

	% of THD obtained by using AWPI	% of THD obtained by using FLC
Inverter Current	13.61%	3.40%
Load Current	13.61%	3.40%
Load Voltage	13.83%	3.87%

Case-2 System operates in modes 3 and 4

	% of THD obtained by using AWPI	% of THD obtained by using FLC
Inverter Current	27.75%	3.40%
Load Current	27.75%	3.40%
Load Voltage	27.75%	3.31%

Case-3 System operates in modes 5, 6, and 7

	% of THD obtained by using AWPI	% of THD obtained by using FLC
Inverter Current	13.06%	3.34%
Load Current	64.94%	3.77%
Load Voltage	6.54%	3.25%

Case-4 Sudden load increment.

	% of THD obtained by using AWPI	% of THD obtained by using FLC
Inverter Current	94.44%	2.64%
Load Current	81.34%	2.84%
Load Voltage	10.14%	3.31%

CONCLUSION

This article describes in depth the study and testing of control mechanisms for a hybrid off-grid system that uses a solar photovoltaic array and VSDG electricity. Findings from the simulation indicate that the system may operate fuel-efficiently when the DE is turned off and the engine is operated at variable speed. It compensates for slow dynamics and maintains system smoothness when operating at different speeds. Simulation and prototype validation have added to the proof that the load can continuously deliver regulated frequency and sinusoidal voltage. It has been shown that the upgraded P&O algorithm, in conjunction with the combined dynamic model of the dc-dc boost converter, achieves optimum performance from the SPA when the amount of sunlight reaching it varies. Further, studies have shown that double-loop control compensates for the slow dynamics of variable speed operation and enhances power management in dynamic scenarios. Additionally, it has been shown that back-calculation techniques used by Fuzzy controllers exhibit resilience. System components such as SPA, BES, load, and DE have their observed conditions coordinated by the nine states of the proposed Fuzzy control approach. Take a look at the statistics to compare the percentages of total harmonic distortion (THD) between the existing controller and the proposed FLC.

REFERENCES

[1] A. Accetta and M. Pucci, “Energy management system in DC micro-grids of smart ships: Main gen-set fuel consumption minimization and fault compensation,” IEEE Trans. Ind. Appl., vol. 55, no. 3, pp. 3097–3113, May/Jun. 2019.

[2] Y. Bhandari, S. Chalise, J. Sternhagen, and R. Tonkoski, “Reducing fuel consumption in microgrids using PV, batteries, and generator cycling,” in Proc . IEEE Int. Conf. Electro-Inf. Technol., 2013, pp. 1–4.

[3] R. É. PeÑa, R. Cárdenas, J. É. Proboste, J. Clare, and G. Asher, “Wind– diesel generation using doubly-fed induction machines,” IEEE Trans. Energy Convers., vol. 23, no. 1, pp. 202–214, Mar. 2008.

[4] S. K. Tiwari, B. Singh, and P. K. Goel, “Control of wind-diesel hybrid system with BESS for optimal

operation," IEEE Trans. Ind. Appl., vol. 55, no. 2, pp. 1863–1872, Mar./Apr. 2019.

[5] M. Greig and J. Wang, "Fuel consumption minimization of variable-speed wound rotor diesel generators," in Proc. 43rd Annu. Conf. IEEE Ind. Electron. Soc., 2017, pp. 8572–8577.

[6] R. Miloud, A. Chandra, B. Singh, and S. Singh, "Microgrid: Configurations, control, and applications," IEEE Trans. Smart Grid, vol. 10, no. 2, pp. 1290–1302, Mar. 2019.

[7] T. Waris and C. V. Nayar, "Variable speed constant frequency diesel power conversion system using doubly-fed induction generator (DFIG)," in Proc. IEEE Power Electron. Specialists Conf., 2008, pp. 2728–2734.

[8] S. Puchalapalli, S. K. Tiwari, B. Singh, and P. K. Goel, "A microgrid based on wind-driven DFIG, DG, and solar PV array for optimal fuel consumption," IEEE Trans . Ind. Appl., vol. 56, no. 5, pp. 4689–4699, Sep./Oct. 2020.

[9] A. K. Birudula, R. Selvaraj, T. R. Chelliah, and U. S. Ramesh, "Improved fuel-use efficiency in diesel-electric tugboats with an asynchronous power generating unit," IEEE Trans. Transp. Electrific., vol. 5, no. 2, pp. 565–578, Jun. 2019.

[10] A. K. Birudula, R. Selvaraj, K. Desingu, T. R. Chelliah, and R. S. Upadhyayula, "A coordinated control strategy for a diesel-electric tugboat system for improved fuel economy," IEEE Trans . Ind. Appl., vol. 56, no. 5, pp. 5439–5451, Sep./Oct. 2020.

[11] N. Mendis, K. M. Muttaqi, S. Perera, and S. Kamalasadan, "An effective power management strategy for a wind-diesel–hydrogen-based remote area power supply system to meet fluctuating demands under generation uncertainty," IEEE Trans. Ind. Appl., vol. 51, no. 2, pp. 1228–1238, Mar./Apr. 2015.

[12] S. Gao, H. Zhao, Y. Gui, D. Zhou, and F. Blaabjerg, "An improved direct power control for doubly fed induction generator," IEEE Trans. Power Electron., vol. 36, no. 4, pp. 4672–4685, Apr. 2021.

[13] R. Cardenas, R. Pena, S. Alepuz, and G. Asher, "Overview of control systems for the operation of DFIGs in wind energy applications," IEEE Trans. Ind. Electron., vol. 60, no. 7, pp. 2776–2798, Jul. 2013.

[14] E. Tremblay, S. Atayde, and A. Chandra, "Comparative study of control strategies for the doubly fed induction generator in wind energy conversion systems: A DSP-Based implementation approach," IEEE Trans. Sustain. Energy, vol. 2, no. 3, pp. 288–299, Jul. 2011.

[15] P. K. Goel, B. Singh, S. S. Murthy, and N. Kishore, "Parallel operation of DFIGs in three-phase four-wire autonomous wind energy conversion system," IEEE Trans. Ind. Appl., vol. 47, no. 4, pp. 1872–1883, Jul./Aug. 2011.

[16] M. Rezkallah et al., "Comprehensive controller implementation for windpv-diesel based standalone microgrid," IEEE Trans. Ind. Appl., vol. 55, no. 5, pp. 5416–5428, Sep./Oct. 2019.